# Automated Fabrication of Streptavidin-Based Self-assembled Materials for High-Content Analysis of Cellular Response to Growth Factors

Julius Sefkow-Werner, Jean Le Pennec, Paul Machillot, Bertin Ndayishimiye, Elaine Castro- Ramirez, João Lopes, Christophe Licitra, Irene Wang, Antoine Delon, Catherine Picart, et al.

# Title

# Automated fabrication of streptavidin-based self-assembled materials for high-content analysis of cellular response to growth factors


## Authors and affiliations

*Julius Sefkow-Werner[1,2], Jean Le Pennec[2], Paul Machillot[2], Bertin Ndayishimiye[2], Elaine Castro-Ramirez[2], Joao Lopes[2], Christophe Licitra[3], Irene Wang[4], Antoine Delon[4], Catherine Picart[1,2,]*, Elisa Migliorini[1,2]**

[1]Univ. Grenoble Alpes, CNRS, Grenoble INP**, LMGP, 38000 Grenoble, France

[2]Univ. Grenoble Alpes, CEA, INSERM, U1292 Biosanté, CNRS EMR 5000 BRM, 38000 Grenoble, France

[3]Univ. Grenoble Alpes, CEA, Leti, F-38000 Grenoble, France

[4]Univ. Grenoble Alpes, CNRS, LiPhy, Grenoble, France

*Co-Corresponding author

Migliorini Elisa, 17 rue des Martyrs, 38016 GRENOBLE

Tel : (33)-04 56 52 93 24

Email:

elisa.migliorini@cea.fr

catherine.picart@cea.fr

** Institute of Engineering Univ. Grenoble Alpes

## Keywords

Automation, biomaterials, biomimicry, growth factors, BMP, glycosaminoglycans, high content studies

## Abstract (300 words max at ACS):

The automation of liquid handling routines offers great potential for fast, reproducible and labor-reduced biomaterials fabrication but also requires the development of special protocols. Competitive systems demand for a high degree in miniaturization and parallelization while maintaining flexibility regarding the experimental design. To day, there are only few possibilities for automated fabrication of biomaterials inside multi-well plates. We have previously demonstrated that streptavidin-based biomimetic platforms can be employed to study cellular behaviors on biomimetic surfaces. So far, these self-assembled materials were made by stepwise assembly of the components using manual pipetting. In this work, we introduce for the first time a fully automated and adaptable workflow to functionalize glass-bottom multi-well plates with customized biomimetic platforms deposited in single wells using a liquid handling robot. We then characterize cell response using automated image acquisition and subsequent analysis. Furthermore, the molecular surface density of the biomimetic platforms was characterized *in situ* using fluorescence-based image correlation spectroscopy. These measurements were in agreement with standard *ex situ* spectroscopic ellipsometry measurements. Thanks to automation, we could do a proof-of-concept to study the effect of heparan sulfate on the bioactivity of bone morphogenetic proteins on myoblast cells, using four different BMPs (2,4,6 and 7) in parallel, at five increasing concentrations. Using such automated self-assembly of biomimetic materials, it

may be envisioned to further investigate the role of a large variety of ECM components and growth factors on cell signaling.

## Introduction

Biomimetic approaches gain influence in the design and fabrication of biomaterials for biomedical applications such as tissue repair and drug screening or in fundamental research when studying the interface between cells and their surrounding extracellular matrix (ECM)[1, 2] . Biomimetics in cellular studies means to model the natural environment of cells as precisely as possible, notably mimicking their surrounding ECM regarding its molecular composition[3] and physical properties[4, 5]. These models help for example to reveal synergies between the ECM components such as glycosaminoglycans (GAGs) and growth factors (GFs) which influence cellular fate[6, 7]. Also spatial proximity between cellular adhesion ligands and GFs[8] as well as matrix elasticity or topography[9] play a role in cell signaling. Various biomaterials to study these parameters in 2D and 3D were extensively reviewed and each of them helps to respond to a specific need[8, 10-12].

Due to high complexity of the ECM models and the need for flexibility in biomaterial design for fundamental research, most of the workflow from fabrication to data analysis is manual and thus time-consuming[13]. This makes these approaches less suitable for high-content studies, which gain popularity in order to test different functionalities of biomaterials. Vasilevich et al. predicted a rising involvement of robotics and automation covering almost the integral workflow of an experiment[14]. The researcher would formulate a precise question, later recover the desired biomaterial and present data to the scientific community, while the central robot takes over the experimental design, biomaterial fabrication, cell culture and data analysis. A recent review summarizes the implementation of automation in research laboratories related to biomimetic modeling of diseases and thus enabling high-content studies[15]. Notably, manual pipetting can be

replaced by automation, with the advantage of saving labor time. Indeed, recent studies showed that manual pipetting accuracy depends on the individual operator and thus decreases data reproducibility[16, 17]. Soft lithography or microcontact printing were already shown to be well suited for a high degree of parallelization and miniaturization by creating PDMS microwells[18], which can further include bioactive compounds[19]. However, the degree of flexibility is limited due to time-consuming design and need for fabrication of new masks. Other techniques are adapted to build high-complexity assemblies or human tissues, including bioprinters to produce spatially controlled 3D tissues[20] and liquid handling robots to produce thin films[17].

Standardized multi-well plates with for example 96 wells offer a degree of miniaturization, which reduces the amount of precious cells like stem cells and expensive molecules, like growth factors and chemokines, while still providing sufficient sample volume and thus are adopted for automated biomaterial fabrication[15]. They are commercially available in different versions with different substrates, mostly plastic and glass, and are compatible with common laboratory equipment, including liquid handling robots, microplate readers and high-content screening microscopes. This makes them candidates for automation over the whole experimental workflow from fabrication, cell seeding, sample preparation, data acquisition and post-treatment[17, 21-23]. Examples of liquid handling robots in industry[24] or of automated cell cultures[25] demonstrate the broad application potential and interest of automation. Regarding biomaterial fabrication, Brooks et al. describe the fabrication of 2D and 3D hydrogels on glass using a liquid handling robot inside 96-well plates and further immobilized ECM proteins[22]. In a previous work by our team, Machillot et al. built up a polyelectrolyte multilayer film inside 96-well plates for cellular studies by executing iterative cycles of incubation and rinsing of the three involved electrolytes using a liquid handling robot[17]. This ensured high reproducibility between the equally functionalized wells and plates but the

loading of bone morphogenetic proteins (BMPs) at different concentrations was still done by hand. Sales et al. further automated the workflow of this system by applying automated microscopy and automated image analysis to perform a high-content screening of cell adhesion and early cell differentiation to four BMPs simultaneously[21]. Eggert et al. recently developed the automated fabrication of hydrogels at the single well level[23]. To our knowledge, this approach has never been applied to self-assembled materials made of several pair of deposited layers.

Another challenge relies in the precise characterization of the functionalization of biomaterials inside the 96-well plates, i.e. *in situ*. For thin assemblies, surface sensitive techniques like quartz crystal microbalance with dissipation monitoring (QCM-D) or spectroscopic ellipsometry (SE), among others, enable to follow binding events *in situ* and to quantify the surface density of molecules built-up on model-substrates[26-29]. However, to date, these techniques are barely adapted to 96-well plate format. Thus, there is a need to use other quantitative characterization methods that can be performed *in situ*.

Fluorescence microscopy reveals only relative intensity changes between different conditions based on labeled molecules of interest[30, 31]. Our group recently further developed image correlation spectroscopy (ICS) to precisely measure the number of labelled molecules on 2D biomaterials[32]. The spatial autocorrelation of confocal images reveals intensity fluctuations and its amplitude indicates the number of molecules per point spread function (PSF) and ICS is thus a suitable tool to characterize biomimetic streptavidin platforms.

In terms of type of biomaterials, thin films or assemblies are often used to biofunctionalize surfaces. Notably, the layer-by-layer technique[33] and the streptavidin-based platforms[28] can provide a high degree of versatility of experimental conditions. Our team previously developed a biomimetic platform based on a streptavidin (SAv) monolayer, built on gold sputtered glass surfaces[6, 28, 34-36].

SAv is commonly used for analytical assays or as antibody conjugate and for biochemical studies of molecular interactions[37]. The high affinity and specificity between SAv and biotin permits to immobilize biotinylated molecules of interest in a highly controlled manner to reveal their specific role on cell fate. We recently used such streptavidin platforms to study the synergy between integrins, the GAG heparan sulfate (iHS) and bone morphogenetic protein 2 (BMP2) adsorbed on iHS, by quantifying cell adhesion and BMP2 signaling (i.e the phosphorylation of the SMAD 1/5/9 proteins early effectors of BMP2 interaction with BMP receptors)[38]. To date, comparable data for the role of HS on BMP4, 6 and 7-mediated SMAD signaling is not available.

In this work, we present for the first time the automated fabrication of customized biomimetic SAv platforms on glass-bottom 96-well plates to study cellular responses to GF-presented *via* HS. The entire workflow from discrete functionalization of each single well of a 96-well plate and subsequent analysis of cellular readouts was fully automated using a liquid handling robot, automated image acquisition and analysis (**Figure 1**). To this end, a custom-made graphical user-interface was designed to allow the operator to individually assign different biomimetic SAv platforms to discrete wells selected by the user, and to define experimental parameters in minutes. As a proof-of-concept, we co-immobilized the adhesion peptide cRGD together with the GAG HS to promote cellular adhesion and to present GFs *via* its natural ligand HS. Using ICS, we quantified *in situ* inside 96-well plates the molecular surface density and homogeneity of the self-assembled material. Using the automated approach, we simultaneously studied increasing concentrations of BMP2, BMP4, BMP6 and BMP7 adsorbed on HS and compared them to the presentation in solution. We selected theses BMPs in view of their role in various biological processes throughout the body[39]. BMP2 is mainly involved in the development of the musculoskeletal system, BMP4 regulates cancer, BMP6 is taking part in the ion metabolism and BMP7 participates fat cell

differentiation[7]. We quantified SMAD1/5/9 phosphorylation in BMP-responsive C2C12 mouse myoblasts[21, 40, 41].

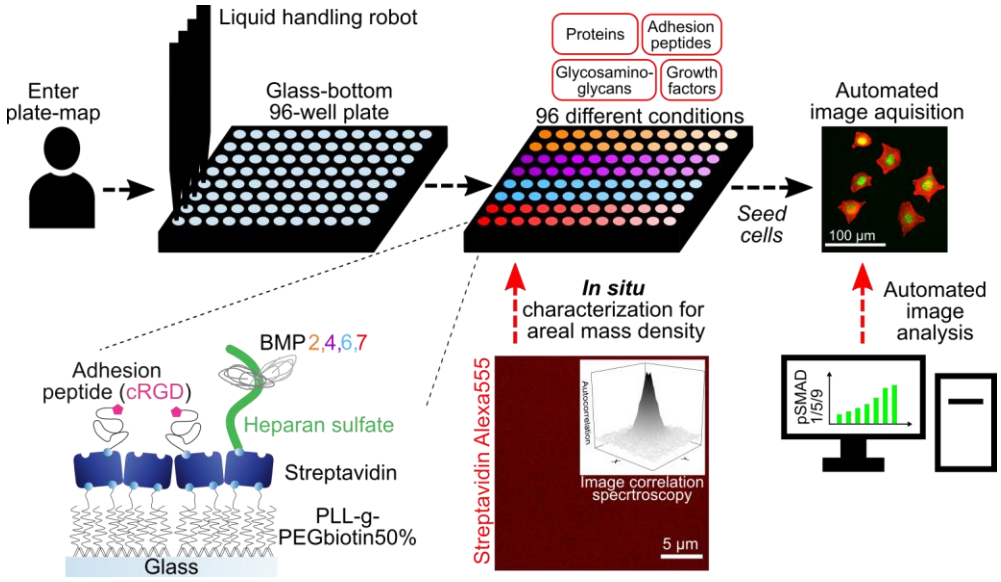


***Figure 1: Schematic of automated platform fabrication, surface characterization and cellular studies****. A user communicates the plate-map corresponding to the experimental plan to the liquid handling robot. Glass bottom 96-well plates are then automatically functionalized with different biomimetic platforms co-presenting cellular adhesion ligands, glycosaminoglycans and growth factors. In this work, streptavidin binds to the linker PLL-g-PEGbiotin50%. Then, biotinylated cRGD and biotinylated heparan sulfate bind to streptavidin and BMP2,4,6 or 7 adsorb to heparan sulfate. The areal mass density of fluorescence labelled molecules such as StreptavidinAlexa555 is characterized in situ using image correlation spectroscopy. Cells are seeded on the platforms for biophysical assays using automated images acquisition and automated image analysis to quantify for example BMP-mediated SMAD1/5/9 phosphorylation inside the nucleus.*

## Methods

### Buffers and molecules

10 mM Hepes 7.2 and 150 mN NaCl buffer (Sigma Aldrich, Saint-Quentin Fallavier, France) named hereafter Hepes was used for dilution and rinsing of all molecules if not further specified. PLL(20)-g[3.5]-PEG(2)/PEGbiotin(3.4)50% (PLL-g-PEGbiotin50%, ~107 kDa, SuSoS AG, Dübendorf, Switzerland) consists of a Poly(L-Lysine) backbone (~20 kDa, ~100 monomers) with one PEG chain (2 kDa) or one PEG biotin chain (3.4 kDa) grafted to one of 3.5 PLL monomers in a 50% ratio. Stock solution (10 µM) was stored at 4 °C for up to 2 months and diluted to 100 nM upon use. Details for SAv (SAv, 55 kDa, Sigma Aldrich, Saint-Quentin Fallavier, France), biotinylated cyclic RGD pentapeptide (cRGD, 3.9 kDa) and biotinylated HS (iHS, 12 kDa) can be found in previous works [36, 38]. Biotinylated Atto565 (bAtto, 922 Da, Sigma Aldrich, Saint-Quentin Fallavier, France). Streptavidin Alexa Fluor® 555 conjugate (SAvAlexa, ~55kDa, Molecular probes, Eugene, Oregon, USA) was used for ICS studies and homogeneity analysis. For some conditions, SAv or SAvAlexa were pre-bound to cRGD at a molar ratio of 3:4 and incubated for 30 min before binding to PLL-g-PEBbiotin50% on the surface. BMP2 (26 kDa, R&D Systems Inc., Minneapolis, Minnesota, USA), BMP4 (24 kDa, Peprotech, Neuilly-Sur-Seine, France), BMP6 (30 kDa, R&D Systems Inc., Minneapolis, Minnesota, USA) and BMP7 (26 kDa, Olympus Biotech, Lyon, France) were serial-diluted to reach the concentrations to bind to iHS or to be added to the cell media.

### Surface functionalization

For *ex situ* characterization, biomimetic platforms were built on silicon dioxide ($SiO_2$) crystals (QSX 303, Biolin scientific, Västra Frölunda, Sweden) for QCM-D measurements and on thermally oxidized silicon wafers coated with a 60 nm-thick $SiO_2$ layer for SE analysis. For *in situ*

characterization and cellular studies, glass-bottom 96-well plates (Greiner bio-one, Les Ulis, France) were used. Substrates were activated using UV/Ozone (ProCleaner Plus, Bioforce Nanosciences, Virginia Beach, Virginia, USA) for 10 min to clean and charge the surface. Molecules were pumped inside a liquid chamber for crystals (QCM-D) and wafers (SE) or pipetted by the liquid-handling robot (Evo 100, Tecan, Männedorf, Switzerland) in case of 96-well plates with the concentrations mentioned in **Table 1**.

### *Ex situ* characterization with quartz crystal micro balance with dissipation monitoring (QCM-D)

To assess the effective deposit on the self-assembled streptavidin-based platform on glass, we used QCM-D (QSense Analyzer, Biolin scientific, Västra Frölunda, Sweden), which allows to follow binding events of the sequential buildup of the biomimetic platform, using $SiO_2$-coated QCM-D crystals.

Dissolved molecules in the concentrations stated in **Table 1** passed through the liquid chamber *via* a peristaltic pump with 15 µl/min (IPC4, Ismatec, Wertheim, Germany) followed by rinsing with Hepes as described in more detail elsewhere[28]. The measured time for a molecule to saturate on the surfaces indicated the incubation time used for each molecule when building-up the biomimetic platforms inside 96-well plates.

### *Ex situ* characterization with spectroscopic ellipsometry (SE)

We used SE (RC2, J.A. Woollam, Lincoln, New England, USA) complementary to QCM-D to measure the mass of molecules of the biomimetic platform *ex situ* on silicon wafers covered with a 60 nm-thick thermal $SiO_2$ layer. Due to optical constraints, it was not possible to use amorphous glass surfaces as in 96-well plates. A peristaltic pump (IPC4, Ismatec, Wertheim, Germany) pumped the molecules or the rinsing buffer Hepes at 100 µl/min into the 500 µl liquid chamber (J.A. Woollam, Lincoln, New England, USA), which was tightly screwed on the wafer.

SE measures the change of the ellipsometric angles Ψ and Δ of polarized light upon changes of the refractive index and thicknesses of optical layers[42]. We measured the $SiO_2$ layer in buffer and fitted its thickness and the angle of incidence offset based on the known optical properties of thermal $SiO_2$ with the J.A. Woollam model SIO2_JAW3 on a fixed 1 nm Intr_JAW3 layer to account for the $SiO_2$/Si interfacial layer[43]. The refractive index for the Hepes buffer was modeled with a Cauchy dispersion law with parameters A set to 1.324, B set to 0.00322 and C set to 0[44]. Molecular adsorption to this base substrate was then modelled using a Cauchy layer where thickness and parameter A were fitted. B was set to 0.00322 and C to 0 [45]. The areal mass density was calculated using the De Feijter equation (2)

$$M = d_A \frac{A_A - A_C}{dn/dc} \quad (1)$$

with $d_A$ as the fitted thickness of the adsorbed layer, $A_A$ its fitted Cauchy parameter A and $A_C$ the Cauchy parameter of the ambient buffer[46]. The corresponding refractive index increments dn/dc relative to water for each molecule were 0.18 (SAv, SAvAlexa, SAvcRGDmix) and 0.158 (PLL-g-PEGbiotin50%, bHS)[47].

## Automated liquid handling

The liquid handling robot was used to fabricate different biomimetic platforms at the bottom of the wells of a 96-well plate. First, the user entered the experimental design of the 96-well plate into a custom-made graphical user interface, defining the corresponding wells and incubation time for each molecule and their position in the compound rack. Each well can thus represent a different biomimetic platform or replicates of those. Then, molecule solutions in their adjusted concentrations (**Table 1**) based on QCM-D measurements and rinsing buffer were placed into racks and up to three UV/ozone-activated 96-well plates were put on the plate carrier. The operating

software of the liquid handling robot executed a custom-made script with the user-entered parameters well selection$_n$ and incubation time$_n$ for each molecule *n* as input. For each of the defined molecules an iterative cycle was run:

1. Aspiration of storage buffer from wells$_n$ to empty the wells
2. Aspiration of solution$_n$ from compound rack position$_n$ and dispense of 60 µl inside well selection$_n$
3. Waiting for incubation time$_n$
4. Rinsing wells$_n$ *via* five loops of dispense and aspiration of rinsing buffer

PLL-g-PEGbiotin50% and biotinylated molecules were incubated much longer than measured since incubation inside wells was static and not under flow as in QCM-D. BMP incubated as long as measured in QCM-D. Plates were then ready for cellular studies and were always used the same day.

### *In situ* characterization inside 96-well plates with optical fluorescence microscopy and ICS

A fluorescence-based approach was used to quantify the homogeneity of glass-bottom 96-well plates functionalized by the robot as well as to measure the areal mass density of different components of the biomimetic platform. SAvAlexa replaced SAv and bAtto served as a representative molecule for the binding of functional biotinylated molecules to SAv.

Wells were functionalized by the robot with PLL-g-PEGbiotin50% followed by either SAvAlexa, SAvAlexa/cRGDmix or SAv and subsequently bAtto in the latter case. The plate was imaged *in situ* with an automated image acquisition system (InCell Analyzer 2500, 20x, Molecular Devices, San Jose, California, USA) for qualitative defect-characterization in the macroscale. These immuno-fluorescence images of the whole well were further treated to remove artefacts due to

uneven illumination or optical constraints. An average image based of at least 20 images not touching the well's border was calculated to represent the acquisition bias. All images of this well were then divided by this average image and in a next step stitched together for a 96-well montage. Intensities were analyzed along a vertical and horizontal line.

To quantify the areal mass density of SAvAlexa and bAtto, a series of ten acquisitions at five different positions throughout the well was taken with a Leica SP8 confocal microscope (Leica, Wetzlar, Germany) using a HC PL APO 63x/1.2 water-immersion objective. The focal plane was identified at maximum intensity, stabilized with automated focus control and a field of 25 µm x 25 µm with 512x512 pixel was imaged with 1% laser intensity at 561nm and 1.2 µs pixel dwell time. Images where then analyzed using the principle of ICS as described elsewhere[32, 48]. In summary, the confocal images were split up into 64 sub-images and the spatial autocorrelation function (ACF) was calculated for each sub-image. This ACF reveals intensity fluctuations and its amplitude is inversely proportional to the number of molecules in the observation area[49]. The observation area is defined by the waist of the point spread function specific for each microscope and the used objective and ranges around 230 nm. An additional photobleaching routine revealed the average number and distribution of fluorophores per molecule and was used to correct the number of molecules by the factor 1.2 for SAvAlexa and 1.09 for bAtto. Representative 63x images were equally contrast treated to retain relative intensity differences.

## Cell culture

To study cellular compatibility of PLL-g-PEGbiotin50%-based biomimetic platforms, C2C12 mouse myoblasts (CRL-1772, ATCC, Manassas, Virginia, USA) were chosen as BMP-responsive reference cells[41]. They were cultured on tissue-treated polystyrene cell culture flasks in Dulbecco's modified Eagle's growth medium (DMEM, Gibco, Illkirch, France) supplemented with 10% heat-

deactivated fetal bovine serum (FBS, PAA Laboratories, Toronto, Canada) and antibiotic-antimycotic (1 %, Gibco, Illkirch, France) at 37 °C and 5 % $CO_2$. Cells were passed at sub-confluency with Trypsin EDTA (Gibco, Illkirch, France) and discarded after 12 passages. Four hours prior to manual seeding onto biomimetic platforms inside 96-well plates, cells were serum starved with FBS-free growth media and then detached from the flask with Accutase (Sigma Aldrich, Saint-Quentin Fallavier, France) and re-suspended in FBS-free growth media.

### C2C12 cell adhesion and differentiation for microcopy analysis

To study cellular adhesion on biomimetic platforms, 31 000 serum starved C2C12 cells per $cm^2$ were plated on functionalized 96-well plates, incubated (37 °C, 5% $CO_2$) and stained with 10 ng/ml Hoechst after 1 h. Cells were imaged using Zeiss Axio Observer 7 epifluorescence microscope (Carl Zeiss Sas, Le Pecq, France) and then rinsed with PBS to remove non-adherent cells before again imaging the remaining cells at the same position. Nuclei were counted using an ImageJ plugin to calculate the percentage of adherent cells.

For the quantification of cellular area and the phosphorylation of SMAD1/5/9 translocated into the nucleus upon BMP2 stimulation, 31 000 serum starved cells per $cm^2$ were plated on functionalized surfaces and sBMP2, 4, 6 and 7 was added into the cell media at increasing concentrations. Cells were incubated (37 °C, 5% $CO_2$), rinsed after 1 h 30 min with PBS and fixed a with 4% paraformaldehyde. Cell membranes were permeabilized with 0.2% (w/v) Triton X-100 (Sigma-Aldrich, Saint-Quentin Fallavier, France) for 3 min and blocked with 3% BSA for 1h. Primary rabbit anti-pSMAD1/5/9 (Cell Signaling Technology, Danvers, Massachusetts, USA) diluted 1:400 in PBS and 3% BSA were incubated overnight at 4 °C. After rinsing, secondary goat anti-rat/rabbit Alexa Fluor 488 (Thermo Fischer Scientific, Illkirch, France), 1:500, F-actin Phalloidin-Rhodamine (Sigma-Aldrich), 1:1000 and DAPI, 1:1000, were incubated for 60 min in PBS and 3%

BSA at RT. 2.5% (w/v) Dapco (Sigma-Aldrich, Saint-Quentin Fallavier, France) in PBS at pH=7.8 was used as anti-fade. Cells were imaged using InCell Analyzer 2500 using the 20x objective on three channels. Images were further analyzed with the automated image analysis software InCarta (Molecular Devices, San Jose, California, USA) as previously described[21]: pSMAD1/5/9 intensity was measured only inside the nucleus under a mask defined by the DAPI signal and background subtracted for at least 50 cells per well.

### Statistical Analysis and data treatment

For cell experiments, each condition was prepared as technical duplicate in two different wells and experiments were repeated in three biological replicates. Means were tested for statistical significance between different conditions with the non-parametric Mann-Whitney test with $p =\leq 0.05$ and based on at least three biological replicates. To calculate the half-maximal effective concentration ($EC_{50}$), data was fitted with Origin using the dose response curve (4-parameter logistic model[50]). For the negative control, we assigned a BMP concentration $10^{-4}$ times lower than the lowest BMP concentration instead of zero. The coefficient of variation (CV) was used as a measure for the overall homogeneity of stitched full-well immunofluorescence images by dividing the standard deviation of its intensity by its mean intensity. Then, the homogeneity is expressed by the mean and standard deviation of the CV over three wells. To assess the reproducibility of the functionalization, the CV of the mean intensity of five confocal images per well of three wells and two independent plates was calculated.

## Results

### *Ex situ* characterization of biomimetic platforms on QCM-D crystals and $SiO_2$–coated wafers

In order to establish the streptavidin-based self-assembled material on glass surfaces, we studied *ex situ* the step-by-step buildup using QCM-D and SE with silica-coated crystals and wafers.

PLL-g-PEGbiotin50% saturated the surface after 30 min with an average frequency shift of -23.4 ± 2.9 Hz (**Figure 2 a**). A positive shift in dissipation of 2.8 ± 0.3 x $10^{-6}$ indicated the deposition of a soft the layer. SAv pre-coupled in solution with the cellular adhesion peptide cRGD at the molar ratio 3:4 saturated after 30 min, decreasing the frequency further by -31.1 ± 2.6 Hz. The study of Zhen et al.[51] showed that the number of available biotin binding sites increased when SAv was pre-linked with a biotinylated molecule, probably due to improved layer organization. iHS bound to the remaining biotin binding sites with -4.6 ± 1.3 Hz and BMP2 (192 nM) adsorbed specifically to iHS with -11.7 ± 2.8 Hz. About 50% of BMP2 was partly removed from iHS when rinsed until equilibrium was reached and we further measured that BMP2 bound only marginally and reversibly to the SAv/cRGDmix (**SI Fig 1 a**). BSA bound non-specifically to $SiO_2$ with 2.5 Hz but the passivation with PLL-g-PEGbiotin50% led to non-measurable BSA binding after all incubation steps (**SI Fig 1 b,c**). Biotinylated molecules bound as well to a plain SAv layer as seen *via* the example of iHS (**Figure 2 a**) and also a sequential functionalization of cRGD, iHS and aBMP2 was feasible but more difficult to control (**SI Fig 1 d**).

We further observed that $SiO_2$ crystals aged from their 3$^{rd}$ regeneration cycle which lead to up to 25% higher molecule adsorption starting with PLL-g-PEGbiotin50% and propagating though the consecutive compounds (**SI Fig 1 c, e**). Data in **Figure 2** was acquired on new crystals while experiments in **SI Fig 1** were conducted on crystals regenerated at least 3 times.

We conclude that the SAv/cRGDmix has the highest potential to bind further functional molecules and is the most practical and straightforward approach for automated platform fabrication since it is more simple than incubating SAv and cRGD sequentially. **Table 1** lists the concentrations and incubation times based on the results obtained using QCM-D. These conditions will be used for *in situ* functionalization of the 96-well plates using the liquid handling robot.

***Table 1: Molecule concentrations and incubation times based on QCM-D measurements.***

| *Compound* | *Abbreviation* | *Concentration (µg/ml )* | *Incubation time for surface saturation (min)* |
|---|---|---|---|
| PLL(20)-g[3.5]-PEG(2)/PEGbiotin(3.4)50% | PLL-g-PEGbiotin50% | 10 | 45 |
| Streptavidin | SAv | 10 | 30 |
| Streptavidin Alexa555 | SAvAlexa | 10 | 30 |
| Biotinylated cyclic arginylglycylaspartic acid | cRGD | 0.25 | 4 min (partly saturated) |
| SAv/cRGDmix in molar ratio 3:4 | SAv/cRGDmix | 10 (SAv) + 1 (cRGD) | 30 for pre-coupling, then 45 for saturation |
| SAvAlexa/cRGDmix in molar ratio 3:4 | SAvAlexa/cRGDmix | 10 (SAvAlexa) + 1 (cRGD) | 30 for pre-coupling, then 45 for saturation |
| biotinylated Atto565 | bAtto | 10 | 30 |
| Biotinylated heparan sulfate | iHS | 10 | 30 |
| Adsorbed BMP2,4,6,7 on iHS | aBMP2,4,6,7 | 0.01 - 10 | 90 - 130 |
| Soluble BMP2,4,6,7 | sBMP2,4,6,7 | 0.005 - 5 | until cell fixation |

We then characterized these platforms with SE on $SiO_2$-coated wafers to measure adsorbed "dry" mass of the immobilized compounds. PLL-g-PEGbiotin50% bound to glass with 119 ± 9 ng/cm$^2$, SAv then with 264 ± 6 ng/cm$^2$ and SAv/cRGDmix with 343 ± 25 ng/cm$^2$ (**Figure 2 c**). To characterize the amount of SAv inside the 96-well plates, we used the *in situ* ICS technique. We first verified if SAvAlexa binds similarly than SAv to PLL-g-PEGbiotin50% by QCM-D (**SI Fig 1 f**). We measured that SAvAlexa bound with a frequency shift of -18.6 Hz ± 0.7 Hz to the PLL-g-PEGbiotin50% layer, that is about 25% less than that of unlabeled SAv (-24.7 ± 2.2 Hz); on the other hand, we observed a higher decrease in dissipation. Plotting both binding curves normalized to the time we observed that molecules saturated after an equivalent time. We thus chose SAvAlexa as a suitable molecule to study the SAv-base-layer homogeneity. We performed also SE to calculate the dry mass adsorption of SAvAlexa and SAvAlexa/cRGDmix, which bound to PLL-g-PEGbiotin(50%) with 253 ± 31 ng/cm$^2$ (**Figure 2 c**) and 315 ± 6 ng/cm$^2$ (**SI Fig 2 a**) respectively.

We demonstrated that it is possible to fabricate complex biomimetic surfaces presenting three different functional molecules on glass surfaces.

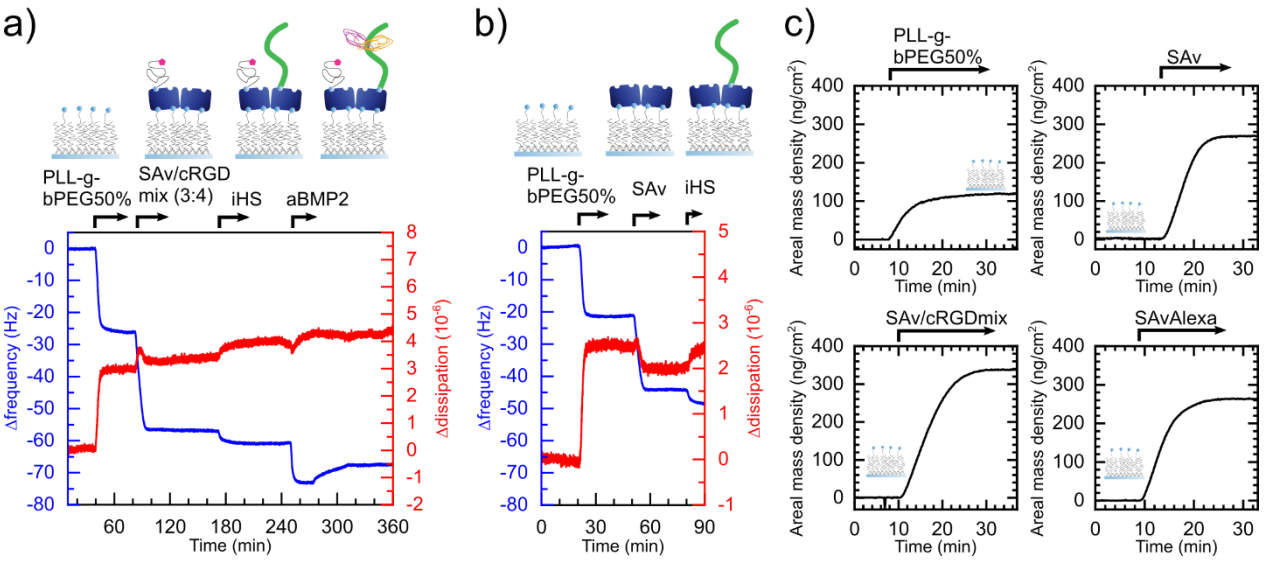


***Figure 2: Ex situ QCM-D and SE characterization of the sequential functionalization of the biomimetic platform*** *a) QCM-D graph showing the frequency change and dissipation change upon the sequential buildup of a biomimetic platform on plasma activated $SiO_2$ crystals. SAv and cRGD were pre-coupled in solution with a molar ratio of 3:4 before binding to the PLL-g-PEGbiotin50% layer. Black arrows indicate periods of incubation followed by rinsing with buffer. b) Graph showing the change in frequency by SAv binding to PLL-g-PEGbiotin50% and iHS occupying the remaining biotin binding sites measured with QCM-D. c) Graph showing the change of the areal mass density of PLL-g-PEGbiotin50% binding to plasma activated $SiO_2$ wafers measured with SE (c, top left). Black arrows indicate time of incubation followed by rinsing with buffer. Areal mass density was calculated using the de Feijter (2) equation based on measured Δthickness and Δrefractive index. The other three panels show SAv, SAv/cRGDmix and SAvAlexa binding to PLL-g-PEGbiotin50%.*

## *In situ* characterization of biomimetic platforms fabricated using a liquid handling robot

Biomimetic platforms were fabricated inside glass-bottom 96-well plates using a liquid handling robot as described above (**Figure 1**). To characterize surface homogeneity and areal mass density *in situ* with fluorescent-based approaches, SAvAlexa was immobilized on PLL-g-PEGbiotin50%. The homogeneity of biotinylated molecules binding to SAv was quantified by immobilizing bAtto on unlabeled SAv in a second incubation step, bAtto binding to the free biotin pockets on SAv. As a third condition, we tested SAvAlexa bound to cRGD with the molar ratio of 3:4 before binding to PLL-g-PEGbiotin50%.

Stitched and shading-corrected 20x fluorescent images of wells acquired with the automated microscope show the global appearance of wells functionalized with the liquid handling robot (**Figure 3 a**). The wells only presented few minor defects. However, in some cases, artefacts were present, such as sickle-shaped black spots (white arrows) at the same place where the tips of the liquid handling robot touched the surface. These were present close to the border of the well. Intensity measurements along a line from left to right and from top to bottom enabled to visualize that SAvAlexa, SAvAlexa/cRGDmix and SAv+bAtto surfaces were globally uniform and reproducible over three different wells (**Figure 3 b**). Tight histograms of the montage of the stitched and shading corrected images further show the uniformity of the wells and their reproducibility (**SI Fig 3 a**). The CV based on intensity distribution of the full well images is in average 3.5 ± 0.7% for SAvAlexa, 6.2 ± 1.7% for SAvAlexa/cRGDmix and 7.3 ± 1.1% SAv+bAtto. We demonstrated that the 96-well plates were homogeneously functionalized with self-assembled streptavidin platforms using the liquid handling robot.

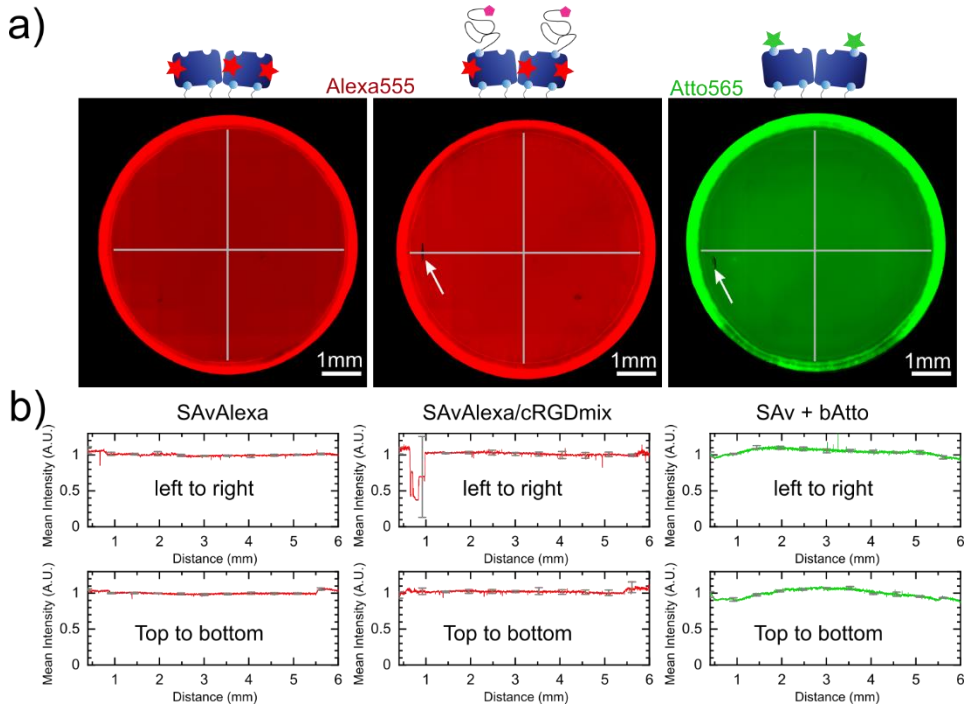


***Figure 3: Homogeneity analysis of indivudal wells of a 96-well plate functionalized using the robot with PLL-g-PEGbiotin50%, SAvAlexa and bAtto*** *a) Representative stitched and shading-corrected 20x IF images of the whole wells presenting different surface functionalization. White arrows indicating the presence of artifacts due to pipetting tips touching the surface. b) Graphs showing the intensity quantification of stitched 96-well images along a line from left to right and top to bottom (n=3 independent wells, error bars=SD).*

Confocal images were acquired to quantify the mass density *in situ* using ICS (**Figure 4**). Representative 63x confocal images showed no systematic defect at the microscale, which is the size of a typical spread cell (**Figure 4 a**). The grain-like structure was then compared to a simulated image based on the random placement of SAvAlexa-like fluorescence emitting entities, which had a similar morphology (**SI Fig 4 a**).

The count rate, which is the measure of mean intensity over three independent wells, revealed a 15% higher signal of SAvAlexa/cRGDmix compared to SAvAlexa (**Figure 4 b**). The bAtto signal

could not be directly compared due to the different fluorophore. The CV based on average intensities was 4% for SAvAlexa, 7% for SAvAlexa/cRGDmix and 25% for bAtto.

The areal mass density of SAvAlexa and bAtto molecules was quantified *in situ* at five different positions. **Figure 4C** gives an example of an ACF over the entire SAvAlexa image. The 25x25-µm greyscale map exemplarily represents the areal mass densities of 64 sub-images for the SAvAlexa sample deduced from the corresponding auto correlation functions (**Figure 4 d**). We applied ICS on the above-mentioned simulated image, which presents a similar theoretical molecular density and equal image size (**SI Fig 4 b-e**). We showed that fluctuations between the sub-images were similar for the simulated image by comparing their CV (**SI Fig 4 e**).

The absolute quantification of the adsorbed mass with ICS *in situ* at five different positions of the well indicated a homogeneous functionalization of SAvAlexa, SAvAlexa/cRGDmix and SAv + bAtto (**Figure 4 e**). SAvAlexa saturated the surface in average with 336 ± 34 ng/cm$^2$ and the SAvAlexa/cRGDmix condition presented an average of 334 ± 45 ng/cm$^2$. Then, 0.79 ± 0.19 ng/cm$^2$ bAtto bound to SAv. To note: bAtto binding could not be measured by QCM-D and neither SE probably due to its low molecular weight and hence low adsorbed mass.

Compared to simple intensity measurements, ICS further revealed information about the fluorescence intensity per molecule, which indicated that SAvAlexa molecules bound to cRGD were brighter than plain SAvAlexa molecules. This might be explained by different spatial organization of these molecules on the surface with an impact on fluorophore efficiency, which did not influence ICS analysis but biased relative intensity comparison between both conditions.

With ICS studies, we succeeded to measure the areal mass density of large and small-labeled molecules *in situ.*

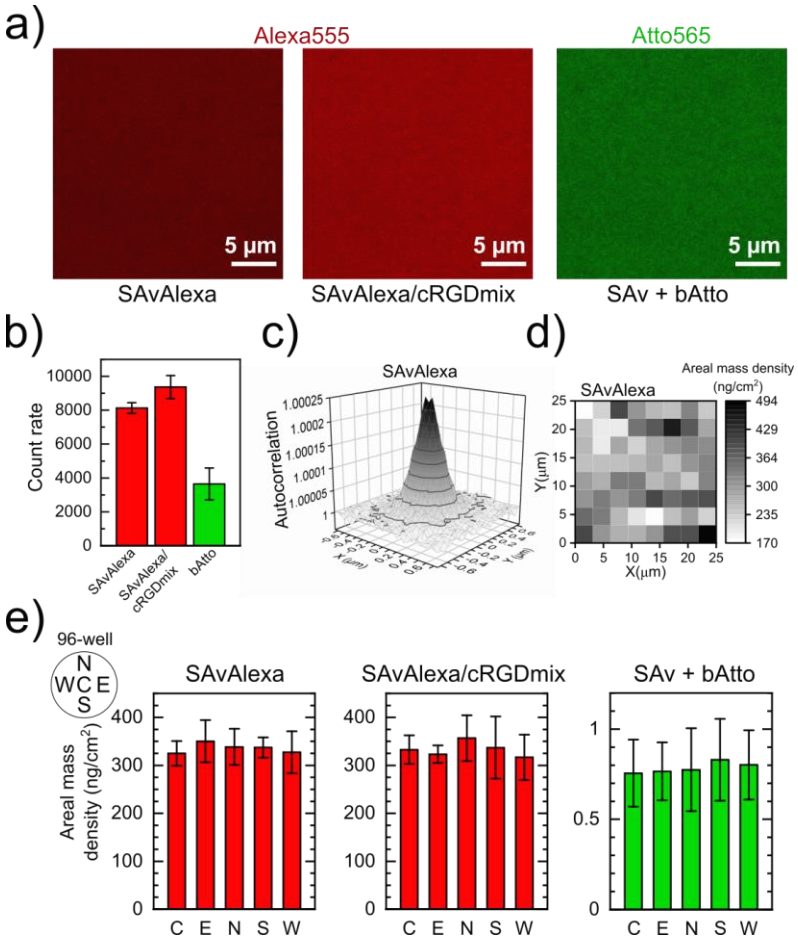


***Figure 4: In situ characterization for areal mass density of SAvAlexa, SAvALexa/cRGDmix and SAvALexa + bAtto.*** *a) Representative 63x confocal images taken inside a single well. b) Graph showing the count rate quantification of 63x confocal images acquired at five positions inside each well (n=3 wells, error bars = SD). c) Exemplary spatial autocorrelation function calculated from the whole image to deduce the number of molecules via its amplitude. d) Representative greyscale map visualizing the areal mass density per sub-image (3.1x3.1µm) measured via ICS. e) Graphs showing the areal mass density via ICS at five different positions per well (n=3 wells, 2 replicates, error bars = SD).*

ICS derived areal mass densities were compared to complementary SE measurements summarized in **Table 2**. The mass of SAvAlexa is the only one directly comparable between both ICS and SE.

ICS is the only technique to measure molecular densities *in situ* inside 96-well plates without passing *via* auxiliary substrates as needed for SE or QCM-D. It is further sufficiently sensitive to measure very small densities as seen with bAtto.

| *Compound* | *Molecular weight(kDa)* | *Mass SE (ng/cm$^2$)* | *Mass ICS (ng/cm$^2$)* |
|---|---|---|---|
| PLL-g-PEGbiotin50% | 107 | 120 ± 8.7 | N.A. |
| SAv | 55 | 263 ± 6 | N.A. |
| SAvAlexa | 55 | 253 ± 33 | 336 ± 34 |
| SAv/cRGDmix 3:4 | N.A. | 343 ± 25 | N.A. |
| SAvAlexa/cRGDmix 3:4 | N.A. | 315 ± 6 | 334 ± 45 |
| bAtto | 0.922 | N.A. | 0.79 ± 0.19 |

***Table 2: Comparison of SE and ICS to measure the areal mass density ex situ and in situ****. The measured mass of SAvAlexa/cRGDmix for ICS presents only the SAvAlexa part whereas for SE the mass of the whole complex is measured. Values are given as mean and SD. ICS measurements were not possible on unlabeled molecules and SE was not sensitive enough to measure bAtto binding. Values are given as mean ± SD over at least 3 replicates.*

## Cellular adhesion and BMP2 signaling on biomimetic platforms in 96-well plates

In order to study BMP-2 mediated cellular responses on C2C12 skeletal myoblasts, we studied the cellular responses on streptavidin-based biomimetic platforms fabricated using the liquid handling robot. We quantified the homogeneity of cell adhesion onto cRGD and also the homogeneity of BMP-2 signaling.

While 86.6 ± 4.2 % of cells adhered to saturated cRGD and spread well, only 10.0 ± 0.1 % remained on bPEG-functionalized surfaces and remained round (**Figure 5 a**). A comparison of cellular adhesion between different positions throughout the well revealed no significant difference (**Figure**

**5 b**). We showed that C2C12 cells adhered specifically to cRGD and homogeneously over the whole surface (**Figure 5 b**).

Platforms functionalized with a sub-monolayer of cRGD and co-functionalized with iHS and aBMP2 (2.5 µg/mL for 90 min) were fabricated and sBMP2 at 100 ng/ml was used as a control. Seeded cells were fixed after 1.5 h and F-actin, nucleus and pSMAD1/5/9 were stained to quantify BMP2 signaling. Cells still spread on platforms with the sub-saturated layer of cRGD with an area of 951 ± 9 $\mu m^2$ and slightly more on the co-functionalized platform with 1009 ± 17 $\mu m^2$.

We quantified homogeneity of BMP2 response by analyzing pSMAD1/5/9 intensity at five positions throughout the surface (**Figure 5 c**). sBMP2 and aBMP2 equally induced SMAD1/5/9 phosphorylation with significant difference to the negative controls and the signal was evenly intense at the five different positions.

We conclude that C2C12 adhesion on PLL-g-PEGbiotin50% based platforms is specific to cRGD and that platforms sequentially built-up by the robot and presenting the functional molecules cRGD, bHS and aBMP2 are homogeneous over the entire well.

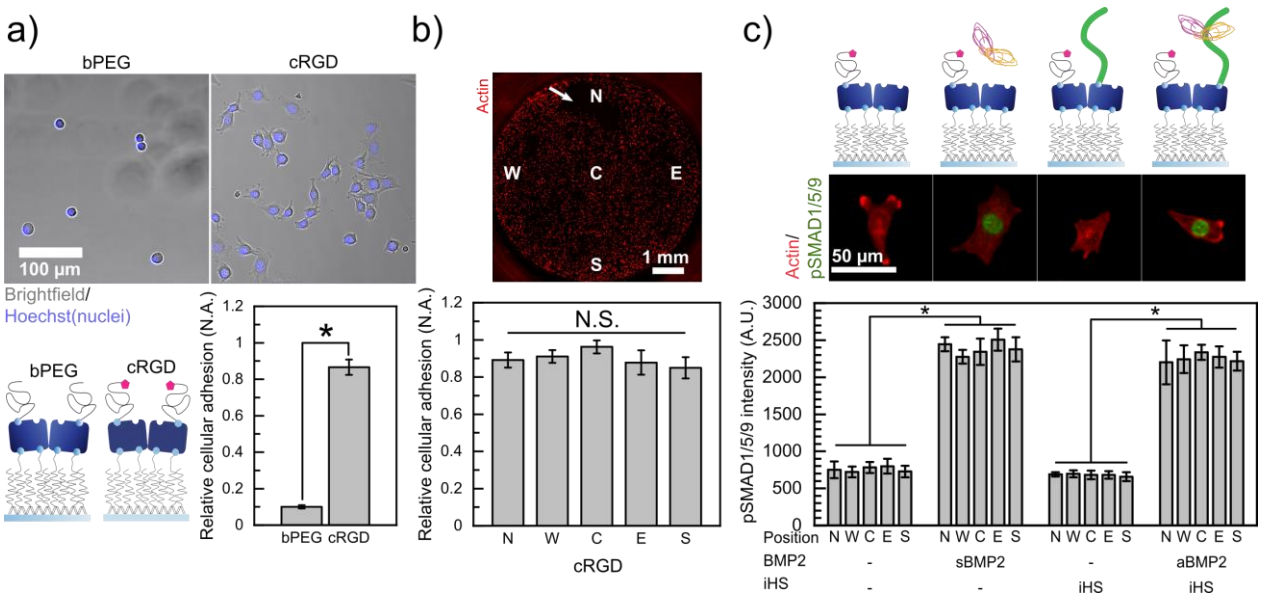


***Figure 5: C2C12 cell adhesion to cRGD and BMP2-induced pSMAD1/5/9 signaling*** *a) Representative bright-field images of C2C12 cells adhering to bPEG and cRGD with graph showing the corresponding quantification of relative cellular adhesion after rinsing. B) Representative stitched 10x Immunofluorescence image of fixed and actin labelled C2C12 cells adhering throughout the whole well. The white arrow indicates rinsing artifacts during staining. Below, a graph shows the quantification of relative cellular adhesion of C2C12 cells on saturated cRGD platforms at five positions throughout the well. C) Automatically acquired representative 24mmune fluorescence images of C2C12 cells on cRGD and/or BMP2-presenting platforms stained for actin and pSMAD1/5/9. Below is a graph showing the pSMAD1/5/9 intensity quantification at five positions throughout the well, processed using automated image analysis software. All experiments were repeated at least 3 times, error bars = SEM and significance was tested with Mann-Whitney for $p \leq 0.05$.*

C2C12 dose response to sBMP2,4,6,7 or aBMP2,4,6,7

We took advantage of the high-content fabrication protocol to study the dose response of C2C12 cells to four different BMPs in parallel by comparing the $EC_{50}$ values. We further studied the effect of HS on BMP signaling. With the liquid handling robot, we functionalized a 96-well plate with 42 different conditions in technical duplicates presenting the BMPs either in solution (sBMP2,4,6,7) or adsorbed on iHS (aBMP2,4,6,7) for 130 min. This approach is easy to use for the experimentalist, a trained user taking only 15 min to enter the experimental parameters *via* the custom-made graphical user interface. We quantified SMAD1/5/9 phosphorylation with automated microscopy and image analysis (**Figure 6 a**).

We identified initial aBMP2,4,6,7 concentrations in a way that all BMPs bound with comparable frequency shifts to iHS before rinsing using QCM-D (**SI Fig 5 a**). These concentrations were high, in the range of 1-10 µg/mL, to induce maximal SMAD1/5/9 phosphorylation. From this BMP2,4,6,7 specific base concentration, we chose a step-wise 100 fold dilution and also added a 10 µg/ml common upper concentration.

The robot functionalized this specific whole plate in 6 h of which roughly 4 h were waiting time for molecule incubation and 2 h liquid handling operations. Automated image acquisition and analysis took one hour each with additional 15 min user interaction for both steps to set up the microscope and to calibrate the image analysis software.

Representative single cell images of the negative control, an intermediate BMP concentration and a plateau condition show pSMAD1/5/9 presence in the nucleus (**Figure 6 b**). For all sBMP2,4,6,7 and aBMP2,4,6,7 conditions, we observed a BMP dose-dependent response in C2C12 cells (**Figure 6 c**). The sBMP2,4,6,7 concentration of 1 µg/ml, which in all cases represented an upper plateau pSMAD1/5/9 signal, was significantly higher than the negative control. Also, when comparing the aBMP2,4,6,7 conditions, the comparable concentration of 3, 5, 10 and 5 µg/ml respectively induced

a plateau pSMAD1/5/9 signal, which was significantly higher than the negative control and comparable to the plateau induced by corresponding sBMP2,4,6 and 7. Statistical significance between intermediate concentrations to the negative control and to either sBMP2,4,6,7 at 1 µg/ml or aBMP2,4,6,7 at 3, 5, 10 or 5 µg/ml was tested.

$EC_{50}$, were calculated from these curves, which corresponds to the BMP concentration for which the pSMAD1/5/9 signal is about 50% of the plateau value (**SI Fig 5 b**). The results of the fits are summarized in **Table 3**. sBMP2 thus was more potent to induce SMAD1/5/9 phosphorylation than sBMP4,6 and 7 which were comparable to each other. In addition, aBMP2 was more bioactive than aBMP4 and aBMP7 but for aBMP6 the fit for the dose response curve failed because at high aBMP6 concentrations the plateau of the pSMAD1/5/9 response was not reached. Hammers et al. measured in a similar experiment with soluble BMPs $EC_{50}$ values for sBMP2,4,6 and 7 **Table 3**[52].

Thus, using the robot, many different conditions could be studied in parallel upon user demand. Together with automated image acquisition and analysis, the workflow appears to be fast and reproducible for high-content studies with a customized biomaterial. Here, we were able to identify sBMP2,4,6,7 and aBMP2,4,6,7 concentrations in the dynamic range of induced SMAD1/5/9 phosphorylation, which allows direct comparison of the BMPs bioactivity. These so-called critical concentrations may further be used to measure the influence of other factors on SMAD1/5/9 phosphorylation, including gene mutations, drugs, receptors or molecules from the extracellular matrix.

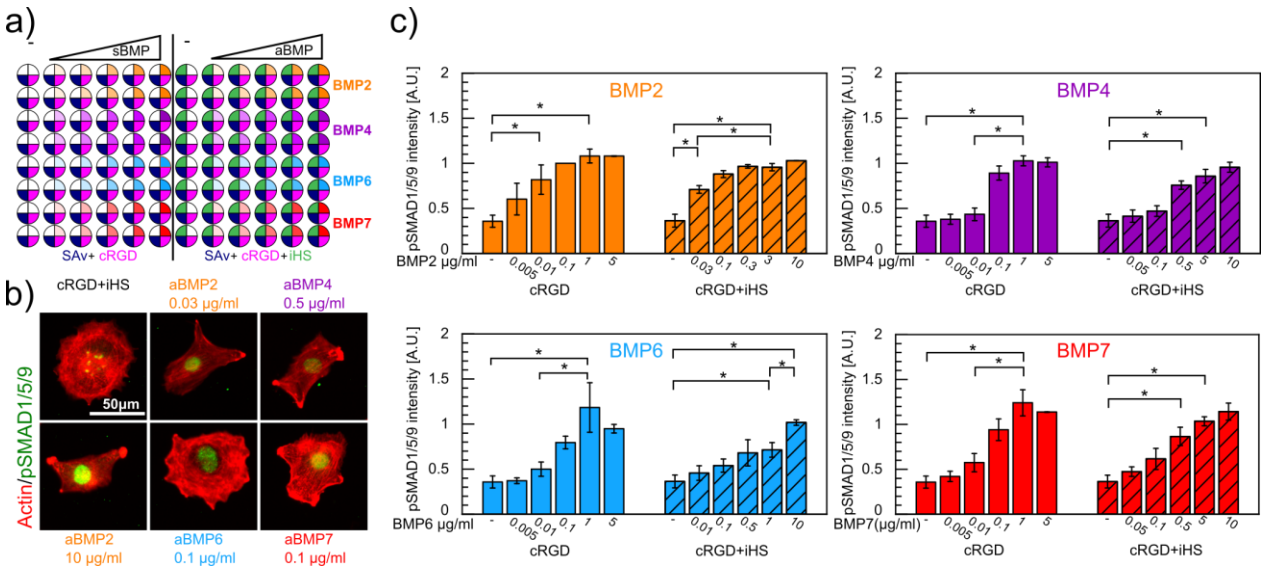


***Figure 6: Automated high-content study of C2C12 cell response to sBMP2,4,6,7 and aBMP2,4,6,7.*** *a) Schematic of a 96-well plate with 42 different conditions in duplicates fully functionalized by the robot. sBMP2,4,6 and 7 in different concentrations were added by hand into the cell media when cells were plated. b) Representative and equally treated images of C2C12 cells plated inside the 96-well plate functionalized by the robot, fixed after 90 min and labelled for actin and pSAMD1/5/9 translocated into the nucleus. BMP concentrations were chosen to represent a condition close to the $EC_{50}$ concentration c) Graphs show the quantification of pSMAD1/5/9 translocated into the nucleus. Values were normalized to the sBMP2 condition at 0.1 µg/ml. Each experiment was the average of two wells and the error bars represent the SEM. Significance was tested with Mann-Whitney and $p < 0.05$ for $n = 3$. The aBMP2,4,6 and 7 concentrations represent the concentrations used for the incubation on iHS and don't permit a quantitative conclusion on the amount of aBMP2/4/6/7 eventually adsorbed on iHS.*

***Table 3: $EC_{50}$ values for sBMP2,4,6 and 7 and aBMP2,4,6 and 7 on cRGD platforms compared to values of a similar study with C2C12 cells on tissue culture plates[52]****. Values are given as mean ± SD over three replicates.*

| | *EC50 ( µg/ml)* | | *EC50 (nM )* | | *EC50 (nM )* |
|---|---|---|---|---|---|
| | *sBMP* | *aBMP* | *sBMP* | *aBMP* | *sBMP [52]* |
| BMP2 (26 kDa) | 0.007 ± 0.001 | 0.028 ± 0.007 | 0.269 ± 0.038 | 1.08 ± 0.27 | 0.033 ± 0.002 |
| BMP4 (24 kDa) | 0.027 ± 0.003 | 0.227 ± 0.033 | 1.13 ± 0.13 | 9.46 ± 1.38 | 0.010 ± 0.0004 |
| BMP6 (30 kDa) | 0.035 ± 0.022 | fit failed | 1.12 ± 0.73 | fit failed | 1.3 ± 0.032 |
| BMP7 (26 kDa) | 0.042 ± 0.011 | 0.294 ± 0.150 | 1.62 ± 0.42 | 11.3 ± 5.77 | 5.9 ± 0.22 |

## Discussion

Here, we presented for the first time the automated functionalization of SAv biomimetic platforms built-up on glass-bottom 96-well plates for cellular studies. To this end, we developed an automated experimental workflow to fabricate on-demand biomimetic platforms using custom-made software, a liquid handling robot and automated image acquisition and analysis. C2C12 cells responded to co-presented cRGD and on iHS adsorbed aBMP2,4,6,7 *via* specific adhesion and SMAD1/5/9 phosphorylation.

Automated liquid handling protocols for self-assembled materials directly inside multi-well plates have been rarely developed before[17], and the previous study did not address single well customization with a large choice of different solutions. The originality here relies in the possibility to assign complex and independent experimental conditions to each individual well. Moreover, it is possible to choose between using few wells only or the plate as a whole, resulting in optimized material consumption and allowing low-content preliminary studies. In addition, the number of replicates is flexible, which is important if different cell types are studied in parallel on identical conditions or different read-outs on the same condition are desired. Lastly, the advantage of using SAv as a base opens this system to a vast field of applications due to its specific affinity to biotin.

By transferring all liquid handling operations to the robot, the user participation in the experiment was reduced by hours depending on the complexity of the experimental plan and a source for human errors was eliminated[16]. Adaptation to other glass-bottom multi-well supports is possible due to the large range of compatible pipetting hardware offered by TECAN but would also come along with further development of the graphical user interface. In addition, cell seeding and adding soluble factors to the media would be feasible with this set-up under the condition that the system is placed under sterile environment.

Here, we applied ICS for the first time to quantify molecular densities in fluorescence confocal images acquired *in situ* in the context of surface characterization of biofilms where this technique is not common[29]. Functionalized surfaces were characterized *in situ* using ICS and compared to results obtained in *ex situ* measurements on model silica substrates using QCM-D and SE.

Calculated number of molecules per observation area translated into mass per area allow direct comparison to measurements acquired with SE (**Table 2**). With SE we were not able to detect the small molecule bAtto binding to SAv whereas with ICS we reproducibly measured 0.79 ± 0.19 ng/cm$^2$. The SE measurements for SAv and SAvAlexa were comparable to each other while the SAvcRGDmix bound with an increase of 80 ng/cm$^2$. Since ICS measurements suggest that the amount of SAvAlexa on the surface in its pure version or coupled to cRGD is similar, the additional mass describes mostly the amount of cRGD on the surface. Interestingly the amount of bAtto bound on SAv layer is more than an order of magnitude lower than the cRGD pre-coupled with SAvAlexa[32]. This may indicate that when we premixed SAv and cRGD we avoided the long PLL-g-PEGbiotin chains from occupying the biotin pockets available on streptavidin, in line with Zhen et al.[51].

ICS derived areal mass densities were comparable to the ones measured with SE with a difference of 32% for SAvAlexa while the standard deviation between replicates ranges around 10-20% for both approaches. We thus validated ICS as a suitable technique to characterize biomimetic SAv platforms *in situ*. One source for this difference can origin from the two different substrates used, glass for ICS and thermal $SiO_2$ for SE. With SE, we measured 120.2 ± 8.7 ng/cm$^2$ PLL-g-PEGbiotin50% and 253.2 ± 32.8 SAvAlexa. Indeed, other studies show that the binding of PLL-g-PEGbiotin depends on the substrate[53]. Huang et al. show that PLL-g-PEGbiotin with different percentages of grafted biotin bind all similar with 2.5 pmol/cm$^2$ (268 ng/cm$^2$ for PLL-g-PEGbiotin50%) to $NbO_2$ to which SAv adsorbed with 369 ng/cm$^2$ [47]. Städler et al. however measured on the same substrate 218 ± 16 ng/cm$^2$ of PLL-g-PEGbiotin with 350 ng/cm$^2$ Neutravidin adsorption[54]. But experiments on $SiO_2$ show 145 ng/cm$^2$ for a PLL-g-PEGbiotin layer and subsequent SAv binding of only 120 ng/cm$^2$ [55].

While ICS avoids passing *via* tools with substrates such as QCM-D, SE, OWLS or *via* indirect measurements (µBCA), it has other constraints: Compounds need to be labelled with a fluorophore, which might alter molecular binding properties and also leads to negligence of un-labelled molecules[56]. While confocal microscopes are abundant in research facilities, specific analysis software to calculate the ACF and to deduce the number of molecules per observation area is scarcely available and analysis relies on custom-made tools, extensions and experienced users. Nevertheless, we proved that this method is more accurate to characterize biomaterials *in situ* than simple relative intensity comparison done with any fluorescent microscopy due to artefacts from varying fluorophore efficiency between samples probably related to quenching (**Figure 4 e, f**)[57].

As proof-of-concept of our functionalization workflow, we studied the dose-response of C2C12 cells to different concentrations of BMP2,4,6,7 in parallel adsorbed to iHS or in soluble condition.

The calculated $EC_{50}$ values proved that BMP2 is the most potent among the four studied GFs in soluble form and adsorbed on HS because it already induces SMAD1/5/9 phosphorylation at lower concentrations. Hammers et al. measured one and two orders of magnitude lower $EC_{50}$ values for sBMP2 and sBMP4 respectively whereas sBMP6 and sBMP7 were comparable[52]. Their use of typical tissue culture plates compared to our cRGD platforms could explain these differences. Sales et al. also compared concentrations of matrix-bound BMP2,4 and 7 to each other and found higher SMAD1/5/9 phosphorylation induced by BMP2 compared to BMP4 and BMP7 at low concentrations[21]. However, at higher concentrations, BMP7 was inducing the highest signal among all. Thanks to the novel workflow here reported it will be possible to perform a systematic study of the effect of different GFs and of different GAGs on cellular signaling.

## Conclusion

We presented an automated workflow for the functionalization at the single well level of a biomimetic self-assembled material inside glass-bottom 96-well plates. With a graphical user interface, we empowered the user to enter a complex experimental set-up in minutes, presenting a maximum of 96 different conditions on the same plate for up to three identical plates in parallel. A custom-made software translated this plan into liquid handling commands, which were executed by a liquid handling robot in a reproducible and homogeneous way. By characterizing the wells with image correlation spectroscopy, we measured the molecular density of biomimetic surfaces *in situ. We did a proof-of-concept and studied the effect of BMP-mediated cell signaling on streptavidin platforms presenting heparan sulfate and four different BMPs.* Cell adhesion and BMP2 mediated signaling were followed using automated image acquisition and subsequent high content analysis. We found that BMP2, 4, 6 and 7 adsorbed at very low concentrations to immobilized heparan sulfate and could induce SMAD1/5/9 phosphorylation, BMP2 being the most

effective. Thus, we demonstrate that it is possible to custom-design multi-well plate for self-assembled materials and to perform parallel studies in the same experimental conditions. Such fabrication method may be used by other researchers to study the synergies between matrix components and growth factors on cellular processes.

## Declaration of Competing Interest

The authors declare that they have no competing financial interests or personal relationships that could have appeared to influence the work reported in this paper.

## Acknowledgements

We acknowledge Dr. Didier Boturyn and Remy Lartia from DCM in Grenoble for the synthesis of the cRGD peptide. For fruitful discussions, we thank Prof. Ralf Richter (Univerity of Leeds), Dr. Liliane Guerente (DCM Grenoble) and Dr. Elisabetta Ada Cavalcanti-Adam (MPI Heidelberg) as well as the members of our group BRM at CEA. Hajar Ajiyel, Marie Dutoit, Samy Idelcadi and Julia Levy from Grenoble INP further contributed to software development. This project received funding from: Fondation Recherche Médicale (No. DEQ20170336746), ANR CODECIDE (No. ANR-17-CE13–022), ANR GlyCON (No. ANR- 19-CE13-0031-01 PRCI) and the Initiative de Recherche Stratégique, University Grenoble Alpes (IDEX- IRS 2018–2021). This work has been supported by CNRS GDR 2088 "BIOMIM", ANR-17-EURE-0003 and GRAL, ERC POC BIOACTIVECOATINGS 2015 (GA692924)

## Literature


1. Mano, J. F.; Choi, I. S.; Khademhosseini, A., Biomimetic Interfaces in Biomedical Devices. *Advanced healthcare materials* **2017,** *6* (15).

2. Curry, A. S.; Pensa, N. W.; Barlow, A. M.; Bellis, S. L., Taking cues from the extracellular matrix to design bone-mimetic regenerative scaffolds. *Matrix biology : journal of the International Society for Matrix Biology* **2016,** *52-54*, 397-412.

3. Hynes, R. O., The extracellular matrix: not just pretty fibrils. *Science (New York, N.Y.)* **2009,** *326* (5957), 1216-9.

4. Engler, A. J.; Sen, S.; Sweeney, H. L.; Discher, D. E., Matrix elasticity directs stem cell lineage specification. *Cell* **2006,** *126* (4), 677-89.

5. Migliorini, E.; Ban, J.; Grenci, G.; Andolfi, L.; Pozzato, A.; Tormen, M.; Torre, V.; Lazzarino, M., Nanomechanics controls neuronal precursors adhesion and differentiation. *Biotechnology and bioengineering* **2013,** *110* (8), 2301-10.

6. Migliorini, E.; Horn, P.; Haraszti, T.; Wegner, S.; Hiepen, C.; Knaus, P.; Richter, P.; Cavalcanti-Adam, E., Enhanced biological activity of BMP-2 bound to surface-grafted heparan sulfate. *Advanced Biosystems* **2017,** *1* (4), 1600041.

7. Migliorini, E.; Guevara-Garcia, A.; Albiges-Rizo, C.; Picart, C., Learning from BMPs and their biophysical extracellular matrix microenvironment for biomaterial design. *Bone* **2020,** *141*, 115540.

8. Monteiro, A. I.; Kollmetz, T.; Malmstrom, J., Engineered systems to study the synergistic signaling between integrin-mediated mechanotransduction and growth factors (Review). *Biointerphases* **2018,** *13* (6), 06d302.

9. Vassey, M. J.; Figueredo, G. P.; Scurr, D. J.; Vasilevich, A. S.; Vermeulen, S.; Carlier, A.; Luckett, J.; Beijer, N. R. M.; Williams, P.; Winkler, D. A.; de Boer, J.; Ghaemmaghami, A.

M.; Alexander, M. R., Immune Modulation by Design: Using Topography to Control Human Monocyte Attachment and Macrophage Differentiation. *Advanced Science* **2020,** *7* (11), 1-9.

10. Nicolas, J.; Magli, S.; Rabbachin, L.; Sampaolesi, S.; Nicotra, F.; Russo, L., 3D extracellular matrix mimics: fundamental concepts and role of materials chemistry to influence stem cell fate. *Biomacromolecules* **2020,** *21* (6), 1968-1994.

11. Pagel, M.; Beck-Sickinger, A. G., Multifunctional biomaterial coatings: Synthetic challenges and biological activity. *Biological chemistry* **2017,** *398* (1), 3-22.

12. He, W.; Reaume, M.; Hennenfent, M.; Lee, B. P.; Rajachar, R., Biomimetic hydrogels with spatial- and temporal-controlled chemical cues for tissue engineering. *Biomaterials science* **2020,** *8* (12), 3248-3269.

13. Eggert, S.; Hutmacher, D. W., In vitro disease models 4.0 via automation and high-throughput processing. *Biofabrication* **2019,** *11* (4).

14. Vasilevich, A.; de Boer, J., Robot-scientists will lead tomorrow's biomaterials discovery. *Current Opinion in Biomedical Engineering* **2018,** *6*, 74-80.

15. Grubb, M. L.; Caliari, S. R., Fabrication approaches for high-throughput and biomimetic disease modeling. *Acta biomaterialia* **2021,** *132* (xxxx), 52-82.

16. Lippi, G.; Lima-Oliveira, G.; Brocco, G.; Bassi, A.; Salvagno, G. L., Estimating the intra- and inter-individual imprecision of manual pipetting. *Clinical Chemistry and Laboratory Medicine (CCLM)* **2017,** *55* (7), 962-966.

17. Machillot, P.; Quintal, C.; Dalonneau, F.; Hermant, L.; Monnot, P.; Matthews, K.; Fitzpatrick, V.; Liu, J.; Pignot-Paintrand, I.; Picart, C., Automated Buildup of Biomimetic Films in Cell Culture Microplates for High-Throughput Screening of Cellular Behaviors. *Advanced materials (Deerfield Beach, Fla.)* **2018,** *30* (27), e1801097.

18. Afshar, M. E.; Abraha, H. Y.; Bakooshli, M. A.; Davoudi, S.; Thavandiran, N.; Tung, K.; Ahn, H.; Ginsberg, H. J.; Zandstra, P. W.; Gilbert, P. M., A 96-well culture platform enables longitudinal analyses of engineered human skeletal muscle microtissue strength. *Scientific reports* **2020,** *10* (1), 1-16.

19. Kaufmann, T.; Ravoo, B. J., Stamps, inks and substrates: Polymers in microcontact printing. *Polymer Chemistry* **2010,** *1* (4), 371-387.

20. Murphy, S. V.; Atala, A., 3D bioprinting of tissues and organs. *Nature biotechnology* **2014,** *32* (8), 773-785.

21. Sales, A.; Khodr, V.; Machillot, P.; Chaar, L.; Fourel, L.; Guevara-Garcia, A.; Migliorini, E.; Albigès-Rizo, C.; Picart, C., Differential bioactivity of four BMP-family members as function of biomaterial stiffness. *Biomaterials* **2022**, 121363.

22. Brooks, E. A.; Jansen, L. E.; Gencoglu, M. F.; Yurkevicz, A. M.; Peyton, S. R.; Multi-dimensional, C.; Biomaterials, P.-b.; Brooks, E. A.; Jansen, L. E.; Gencoglu, M. F.; Yurkevicz, A. M.; Shelly, R.; Peyton, S. R., Complementary, semiautomated methods for creating multidimensional PEG-based biomaterials. *ACS Biomaterials Science and Engineering* **2018,** *4* (2), 707-718.

23. Eggert, S.; Kahl, M.; Bock, N.; Meinert, C.; Friedrich, O.; Hutmacher, D. W., An open-source technology platform to increase reproducibility and enable high-throughput production of tailorable gelatin methacryloyl (GelMA) - based hydrogels. *Materials and Design* **2021,** *204*, 109619-109619.

24. Zeng, W.; Guo, L.; Xu, S.; Chen, J.; Zhou, J., High-throughput screening technology in industrial biotechnology. *Trends in Biotechnology* **2020,** *38* (8), 1-19.

25. Kletzmayr, A.; Clement Frey, F.; Zimmermann, M.; Eberli, D.; Millan, C., An automatable hydrogel culture platform for evaluating efficacy of antibody-based therapeutics in overcoming chemoresistance. *Biotechnology Journal* **2020,** *15* (5), 1-11.

26. Reviakine, I.; Johannsmann, D.; Richter, R. P., Hearing what you cannot see and visualizing what you hear. *Analytical chemistry* **2011,** *83*, 8838-8848.

27. Dubacheva, G. V.; Araya-Callis, C.; Geert Volbeda, A.; Fairhead, M.; Codée, J.; Howarth, M.; Richter, R. P., Controlling multivalent binding through surface chemistry: Model study on streptavidin. *Journal of the American Chemical Society* **2017,** *139* (11), 4157-4167.

28. Migliorini, E.; Thakar, D.; Sadir, R.; Pleiner, T.; Baleux, F.; Lortat-Jacob, H.; Coche-Guerente, L.; Richter, R. P., Well-defined biomimetic surfaces to characterize glycosaminoglycan-mediated interactions on the molecular, supramolecular and cellular levels. *Biomaterials* **2014,** *35* (32), 8903-15.

29. Migliorini, E.; Weidenhaupt, M.; Picart, C., Practical guide to characterize biomolecule adsorption on solid surfaces (Review). *Biointerphases* **2018,** *13* (6), 06d303.

30. Waters, J. C.; Wittmann, T., Chapter 1 - Concepts in quantitative fluorescence microscopy. Waters, J. C.; Wittman, T., Eds. Academic Press: 2014; Vol. 123, pp 1-18.

31. Galush, W. J.; Nye, J. A.; Groves, J. T., Quantitative fluorescence microscopy using supported lipid bilayer standards. *Biophysical journal* **2008,** *95* (5), 2512-2519.

32. Sefkow-Werner, J.; Migliorini, E.; Picart, C.; Wahyuni, D.; Wang, I.; Delon, A., Combining fluorescence fluctuations and photobleaching to quantify surface density. *arXiv* **2021,** (physics.bio-ph).

33. Gribova, V.; Auzely-Velty, R.; Picart, C., Polyelectrolyte Multilayer Assemblies on Materials Surfaces: From Cell Adhesion to Tissue Engineering. *Chemistry of Materials* **2012,** *24* (5), 854-869.

34. Migliorini, E.; Thakar, D.; Kuhnle, J.; Sadir, R.; Dyer, D. P.; Li, Y.; Sun, C.; Volkman, B. F.; Handel, T. M.; Coche-Guerente, L.; Fernig, D. G.; Lortat-Jacob, H.; Richter, R. P., Cytokines and growth factors cross-link heparan sulfate. *Open biology* **2015,** *5* (8).

35. Amin, L.; Ercolini, E.; Shahapure, R.; Migliorini, E.; Torre, V., The role of membrane stiffness and actin turnover on the force exerted by DRG lamellipodia. *Biophysical journal* **2012,** *102* (11), 2451-60.

36. Thakar, D.; Dalonneau, F.; Migliorini, E.; Lortat-Jacob, H.; Boturyn, D.; Albiges-Rizo, C.; Coche-Guerente, L.; Picart, C.; Richter, R. P., Binding of the chemokine CXCL12alpha to its natural extracellular matrix ligand heparan sulfate enables myoblast adhesion and facilitates cell motility. *Biomaterials* **2017,** *123*, 24-38.

37. Nguyen, B.; Tanious, F. A.; Wilson, W. D., Biosensor-surface plasmon resonance: Quantitative analysis of small molecule-nucleic acid interactions. *Methods* **2007,** *42* (2), 150-161.

38. Sefkow-Werner, J.; Machillot, P.; Sales, A.; Castro-Ramirez, E.; Degardin, M.; Boturyn, D.; Cavalcanti-Adam, E.-A.; Albiges-Rizo, C.; Picart, C.; Migliorini, E., Heparan sulfate co-immobilized with cRGD ligands and BMP2 on biomimetic platforms promotes BMP2-mediated osteogenic differentiation. *Acta biomaterialia* **2020**.

39. Salazar, V. S.; Gamer, L. W.; Rosen, V., BMP signalling in skeletal development, disease and repair. *Nature reviews. Endocrinology* **2016,** *12* (4), 203-21.

40. Sieber, C.; Kopf, J.; Hiepen, C.; Knaus, P., Recent advances in BMP receptor signaling. *Cytokine & growth factor reviews* **2009,** *20* (5-6), 343-55.

41. Katagiri, T.; Yamaguchi, A.; Komaki, M.; Abe, E.; Takahashi, N.; Ikeda, T.; Rosen, V.; Wozney, J. M.; Fujisawa-Sehara, A.; Suda, T., Bone morphogenetic protein-2 converts the differentiation pathway of C2C12 myoblasts into the osteoblast lineage. *The Journal of cell biology* **1994,** *127* (6 Pt 1), 1755-66.

42. Richter, R. P.; Rodenhausen, K. B.; Eisele, N. B.; Schubert, M., Coupling Spectroscopic Ellipsometry and Quartz Crystal Microbalance to Study Organic Films at the Solid--Liquid Interface. Hinrichs, K.; Eichhorn, K.-J., Eds. Springer International Publishing: Cham, 2018; pp 391-417.

43. Herzinger, C. M.; Johs, B.; McGahan, W. A.; Woollam, J. A.; Paulson, W., Ellipsometric determination of optical constants for silicon and thermally grown silicon dioxide via a multi-sample, multi-wavelength, multi-angle investigation. *Journal of Applied Physics* **1998,** *83* (6), 3323-3336.

44. Carton, I.; Brisson, A. R.; Richter, R. P., Label-free detection of clustering of membrane-bound proteins. *Analytical chemistry* **2010,** *82* (22), 9275-81.

45. Cauchy, A. L., *Mémoire sur la dispersion de la lumière*. chez J. G. Calve: Prague, 1836; p IV, 236 S. ; 26 cm CN-ETH-Bibliothek Zürich, Ra.

46. De Feijter, J. A.; Benjamins, J.; Veer, F. A., Ellipsometry as a tool to study the adsorption behavior of synthetic and biopolymers at the air–water interface. *Biopolymers* **1978,** *17* (7), 1759-1772.

47. Huang, N.-P.; Vörös, J.; De Paul, S. M.; Textor, M.; Spencer, N. D., Biotin-Derivatized Poly(l-lysine)-g-poly(ethylene glycol): A Novel Polymeric Interface for Bioaffinity Sensing. *Langmuir : the ACS journal of surfaces and colloids* **2002,** *18* (1), 220-230.

48. Mets, R. D.; Wang, I.; Gallagher, J.; Destaing, O.; Balland, M.; Delon, A. In *Determination of protein concentration on substrates using fluorescence fluctuation microscopy*, 2014/03//.

49. Petersen, N. O.; Höddelius, P. L.; Wiseman, P. W.; Seger, O.; Magnusson, K. E., Quantitation of membrane receptor distributions by image correlation spectroscopy: concept and application. *Biophysical journal* **1993,** *65* (3), 1135-1146.

50. Sebaugh, J. L., Guidelines for accurate EC50/IC50 estimation. *Pharmaceutical Statistics* **2011,** *10* (2), 128-134.

51. Zhen, G.; Eggli, V.; Vörös, J.; Zammaretti, P.; Textor, M.; Glockshuber, R.; Kuennemann, E., Immobilization of the Enzyme β-Lactamase on Biotin-Derivatized Poly( <scp>l</scp> -lysine)- g -poly(ethylene glycol)-Coated Sensor Chips: A Study on Oriented Attachment and Surface Activity by Enzyme Kinetics and in Situ Optical Sensing. *Langmuir : the ACS journal of surfaces and colloids* **2004,** *20* (24), 10464-10473.

52. Hammers, D. W.; Merscham-Banda, M.; Hsiao, J. Y.; Engst, S.; Hartman, J. J.; Sweeney, H. L., Supraphysiological levels of <scp>GDF</scp> 11 induce striated muscle atrophy. *EMBO Molecular Medicine* **2017,** *9* (4), 531-544.

53. Kenausis, G. L.; Vörös, J.; Elbert, D. L.; Huang, N.; Hofer, R.; Ruiz-Taylor, L.; Textor, M.; Hubbell, J. A.; Spencer, N. D., Poly(L-lysine)-g-poly(ethylene glycol) layers on metal oxide surfaces: Attachment mechanism and effects of polymer architecture on resistance to protein adsorption. *Journal of Physical Chemistry B* **2000,** *104* (14), 3298-3309.

54. Städler, B.; Falconnet, D.; Pfeiffer, I.; Höök, F.; Vörös, J., Micropatterning of DNA-tagged vesicles. *European Cells and Materials* **2004,** *7* (SUPPL.1), 86-86.

55. Marie, R.; Dahlin, A. B.; Tegenfeldt, J. O.; Höök, F., Generic surface modification strategy for sensing applications based on Au/SiO 2 nanostructures. *Biointerphases* **2007,** *2* (1), 49-55.

56. Cooper, M., *Label-free biosensors: Techniques and applications*. Cambridge University Press: Cambridge, 2009.

57. Bae, W.; Yoon, T. Y.; Jeong, C., Direct evaluation of self-quenching behavior of fluorophores at high concentrations using an evanescent field. *PloS one* **2021,** *16* (2 February 2021), 1-8.